Journal of Astronomical Telescopes, Instruments, and Systems

AstronomicalTelescopes.SPIEDigitalLibrary.org

Ground-based x-ray calibration of the Astro-H/Hitomi soft x-ray telescopes

Ryo Iizuka
Takayuki Hayashi
Yoshitomo Maeda
Manabu Ishida
Kazuki Tomikawa
Toshiki Sato
Naomichi Kikuchi
Takashi Okajima
Yang Soong
Peter J. Serlemitsos
Hideyuki Mori
Takanori Izumiya
Sari Minami

SPIE.

Ryo Iizuka, Takayuki Hayashi, Yoshitomo Maeda, Manabu Ishida, Kazuki Tomikawa, Toshiki Sato, Naomichi Kikuchi, Takashi Okajima, Yang Soong, Peter J. Serlemitsos, Hideyuki Mori, Takanori Izumiya, Sari Minami, "Ground-based x-ray calibration of the Astro-H/Hitomi soft x-ray telescopes," *J. Astron. Telesc. Instrum. Syst.* **4**(1), 011213 (2018), doi: 10.1117/1.JATIS.4.1.011213.

Ground-based x-ray calibration of the Astro-H/Hitomi soft x-ray telescopes

Ryo Iizuka,[a,*] Takayuki Hayashi,[b,c] Yoshitomo Maeda,[a] Manabu Ishida,[a] Kazuki Tomikawa,[a,d] Toshiki Sato,[a,d] Naomichi Kikuchi,[a,d] Takashi Okajima,[b] Yang Soong,[b] Peter J. Serlemitsos,[b] Hideyuki Mori,[b] Takanori Izumiya,[e] and Sari Minami[f]

[a]ISAS/JAXA, Sagamihara, Kanagawa, Japan
[b]NASA/GSFC, Greenbelt, Maryland, United States
[c]Nagoya University, Chikusa, Nagoya, Aichi, Japan
[d]Tokyo Metropolitan University, Hachioji, Tokyo, Japan
[e]Chuo University, Tokyo, Japan
[f]Nara Women's University, Kitauoya, Nishimachi, Nara, Japan

Abstract. We present the summary of the on-ground calibration of two soft x-ray telescopes (SXT-I and SXT-S), developed by NASA's Goddard Space Flight Center (GSFC), onboard Astro-H/Hitomi. After the initial x-ray measurements with a diverging beam at the GSFC 100-m beamline, we performed the full calibration of the x-ray performance, using the 30-m x-ray beamline facility at the Institute of Space and Astronautical Science of Japan Aerospace Exploration Agency in Japan. We adopted a raster scan method with a narrow x-ray pencil beam with a divergence of ~15″. The on-axis effective area (EA), half-power diameter, and vignetting function were measured at several energies between 1.5 and 17.5 keV. The detailed results appear in tables and figures in this paper. We measured and evaluated the performance of the SXT-S and the SXT-I with regard to the detector-limited field-of-view and the pixel size of the paired flight detector, i.e., SXS and the SXI, respectively. The primary items measured are the EA, image quality, and stray light for on-axis and off-axis sources. The accurate measurement of these parameters is vital to make the precise response function of the ASTRO-H SXTs. This paper presents the definitive results of the ground-based calibration of the ASTRO-H SXTs. [DOI: 10.1117/1.JATIS.4.1.011213]

Keywords: Astro-H; soft x-ray telescope; raster scan; calibration; testing; optical performance.

Paper 17031SSP received Jul. 9, 2017; accepted for publication Jan. 19, 2018; published online Feb. 19, 2018.

1 Introduction

Astro-H is a joint Japan Aerospace Exploration Agency (JAXA)/NASA x-ray satellite launched on February 17, 2016.[1–4] The Astro-H has several instruments to cover a wide energy range from a few hundred eV to 600 keV. It is equipped with two soft x-ray telescopes (SXTs) covering up to about 15 keV.[5,6] One of the two SXTs is for the soft x-ray spectroscopy (SXS: x-ray microcalorimeter detector) for high-resolution spectroscopy. The detector-limited field-of-view (FoV) of the SXS is 3.05 arc min^2, comprising 6×6 pixels. The other SXT is for the soft x-ray imaging (SXI: x-ray CCD detector) for general x-ray spectroscopy. The detector-limited FoV of the SXI is very wide and 38 arc min^2, comprising 1280×1280 pixels.

The Astro-H SXTs are designed on the same basis as those built for the telescopes (XRT-Is) onboard Suzaku, launched in 2007.[7] In order to achieve high throughput within a limited weight allowance, as many aluminum foils as possible, each of which is 101.6 mm long and is 0.15 to 0.31 mm thick, are nested within geometrical constraints. Each telescope consists of 203 nested shells of segmented thin-foil reflectors with a 200-nm gold, epoxy-replicated mirror surfaces, installed in primary and secondary mirror housings. The weight is 43 kg/telescope, which is very light for the achieved effective area (EA). On the other hand, it is difficult to retain all the reflectors in the ideal shapes required by the original Wolter-I optics. We approximated both the primary and secondary reflectors by cones.

The design parameters of the SXT-I and SXT-S are identical and summarized in Table 1. The system requirements are listed in Table 2. Each SXT is composed of the identically designed four "quadrants." Each quadrant comprises primary and secondary housings, which contain reflectors. The reflectors in each housing are supported by seven alignment bars on the top and bottom sides. The precollimator is installed for stray-light protection, which consists of coaxially nested cylindrical aluminum blades placed above each reflector.[8] A thermal shield is attached in front of the precollimator to stabilize the thermal environment of the SXTs.[9] The shield is made of Al-coated 0.2 μm thick polyimide film (PI) to ensure a large EA in the soft energy band.

Figure 1 shows the photos of the Astro-H SXT flight-models. The SXTs were developed at NASA/GSFC. The full details on the design concept, expected performance, fabrication, and interface to the satellite are described in Refs. 5 and 10.

On ground, two measurement methods have been applied for the calibration of the telescope. One is the diverging beam illuminating the full aperture of the telescope (e.g., Ref. 11), where as the other is the raster scan with the pencil beam (e.g., Ref. 12). The full-aperture-illumination with the diverging beam with a long distance source such as the MSFC's XRCF facility and the Panter facility well works to calibrate the image of a high-angular-resolution "arc sec" telescope, such as the

*Address all correspondence to: Ryo Iizuka, E-mail: iizuka@astro.isas.jaxa.jp

Table 1 Design parameters of the Astro-H SXTs.

Design parameter	Suzaku XRT	ASTRO-H SXT
Number of telescopes	4/1 (XRT-I/XRT-S)	1/1 (SXT-I/SXT-S)
Focal length	4.75/4.5 m	5.6 m
Effective diameter	116 to 400 mm	116 to 450 mm
Grazing angle range	0.18 to 0.60/0.19 to 0.64 deg	0.15 to 0.57 deg
Number of nesting	175/168	203
Foil length	101.6 mm	101.6 mm
Reflector layer thickness		
Reflecting surface	Au (0.2 μm)	Au (0.2 μm)
Coupling layer	Epoxy (20 μm)	Epoxy (12 μm)
Reflector substrate	Al (152 μm)	Al (152, 229, 305 μm)
Reflector thickness		
Inner	0.16 mm	0.16 mm (No. 1–79)
Middle	0.16 mm	0.24 mm (No. 80–153)
Outer	0.16 mm	0.32 mm (No. 154–203)
Precollimator		
Blade thickness	Al (0.12 mm)	Al (0.12 mm)
Blade length	30 mm	65 mm
Thermal shield thickness	Al (30 nm) + PI (0.2 μm)	Al (30 nm) + PI (0.2 μm)
Mass of a telescope	~20 kg	~43 kg

Table 2 System requirement of the Astro-H SXTs.

Requirement	Values
EA per telescope	
1 keV	>450 cm^2
6 keV	>390 cm^2
Image quality	
Minimum	<1.7′
Goal	1.3′
FoV[a]	
6 keV	35′

[a]FoV here is defined as the FWHM of the vignetting function for the infinitely wide detector (i.e., the SXT FoV).

Chandra HRMA (e.g., Ref. 13) and the XMM-Newton telescope (e.g., Ref. 11). The pencil-beam raster scan gives a precise solution for the EA calibration since the diverging angle of the beam is quite small, typically tens of arc secs are much smaller than the telescope vignetting. The EA taken with the raster scan method is known as well consistent with that obtained in orbit (e.g., Refs. 7 and 14). Also, the image with an "arc min" angular resolution can be made with the scan (e.g., Ref. 15).

The initial ground calibration was performed at the 100-m beamline at NASA/GSFC, using a diverging beam, and the angular resolutions at 8.0 keV were determined to be 1.1′ and 1.0′ in a half-power diameter (HPD) for SXT-I and SXT-S, respectively.[16] We later conducted the comprehensive ground calibration at the 30-m x-ray beam facility at the Institute of Space and Astronautical Science (ISAS)/JAXA, Japan. We adopted a raster scan method with a narrow x-ray pencil beam with a divergence of 15″.

In this paper, we report the summary of the ground calibration of the Astro-H SXTs at ISAS/JAXA. In Sec. 2, we describe the measurement system at ISAS. The results of the EA, image quality, and stray light are presented in Secs. 3, 4, and 5, respectively. We also compare the results with those of the Suzaku XRT-Is.

2 Measurement Setup

Figure 2 shows a schematic view of the x-ray beam facility at ISAS/JAXA. The measurements are carried out by scanning the SXT aperture with a parallel narrow x-ray beam as follows. To archive high parallelism, we place an x-ray generator at one end of the system and collimate the beam with the slit placed 27 m away from the x-ray source. The resultant beam is highly parallel with the size of 2 mm^2, and the beam divergence is square, ~15″ on each side. To illuminate the entire aperture of the SXT by the fixed x-ray pencil beam, SXTs and detectors are moved synchronously. In addition, thin metal filters and double-crystal monochromator are installed in the beam path in order to obtain monochromatic x-rays.

The same ISAS facility has been also used for the calibration of the x-ray telescopes of Suzaku. The measurement system for Astro-H is almost identical except for two minor changes; the chamber of the sample stage is larger and longer, and the image detector was renewed for the Astro-H calibration. For the focal plane detectors, charge-coupled device (CCD) and proportional counter (PC) are used. The FoV of the CCD is $17.1' \times 15.9'$ (1240×1152 pixels) at the distance of 5.6 m. The size of the PC is 12 mmΦ (7.4′ at 5.6 m). The CCD is used for investigating the image quality, whereas the PC is used for the EA. The details of the raster scan and beam facility are described in Refs. 17–19.

The coordinate system is defined as in Fig. 2. The x-axis is defined to align with the x-ray beam direction. The z-axis is perpendicular to the ground, with the positive direction being upward. The y-axis is on the horizontal plane, and so the three axes form a right-hand coordinate system. The EA and the image quality are measured with raster scan at each quadrant. The four quadrants in each telescope are named Q1, Q2, Q3, and Q4. In this paper, a quadrant coupled with the measured configuration of the coordinates is referred to as $Qn(\pm A)$, where n is the quadrant number of 1 to 4 and A is either Y or Z for the axis; for example, $Q1(+Z)$ means the Q1 with the positive Z-axis configuration.

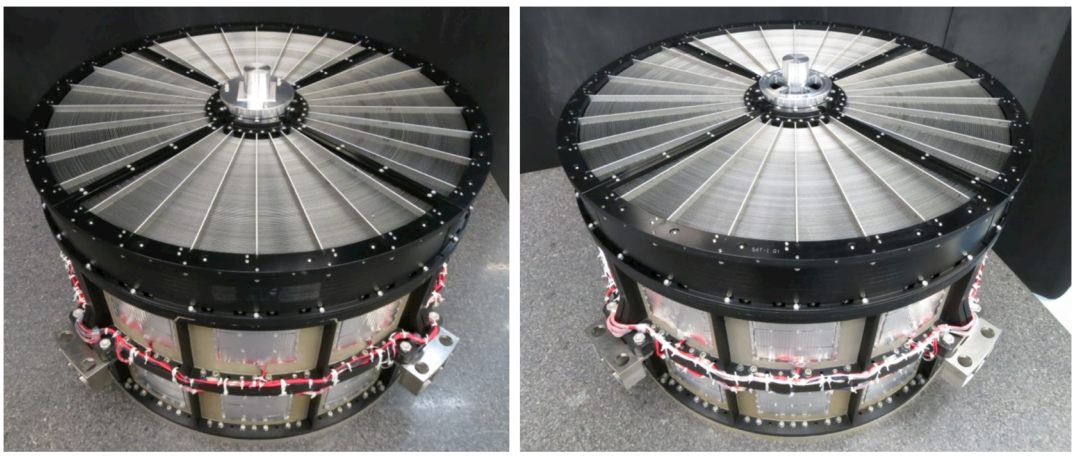

Fig. 1 Flight modules of the Astro-H SXTs (a) SXT-I and (b) SXT-S. The thermal shield is not installed in these figures.

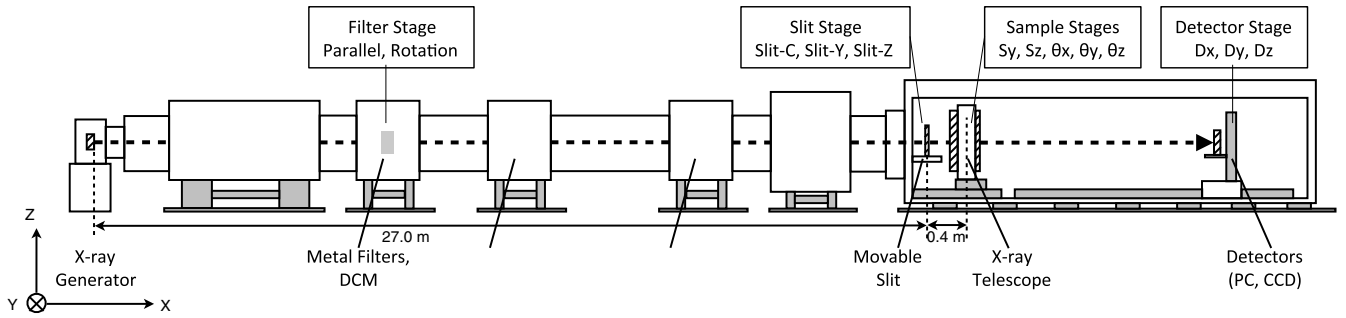

Fig. 2 Schematic view of the ISAS x-ray beam facility. DCM, double-crystal monochromator; PC, proportional counter; CCD, charge-coupled device. Details are given in the Ref. 17.

A dummy frame with the same shape of the thermal shield is installed at the measurement. The thermal shield is a forward-end component of the SXT that plays a role in the thermal shielding to the space. A structure of the frame obstruct a large fraction of the photons at the end sectors and less at the others. The dummy frame has no film or mesh. The mesh works as a neutral density filter in x-rays, whereas the film with the constant thickness uniformly absorbs incoming x-rays. The reduction of the EA due to the film or the mesh is not included in our measurements but was then modeled in our calculation. The errors quoted in this paper are at 1σ confidence level for one parameter of interest.

3 Effective Area

The EA $S_{\rm eff}(E)$ is given by

$$S_{\rm eff} = \frac{v_y h_z C_{\rm scan}}{I}, \tag{1}$$

where v_y and h_z are the scanning speed in the y direction and the scanning pitch in the z direction, respectively, I is the photon count rate of the incident beam, and $C_{\rm scan}$ is the number of the collected photons from all the raster scan paths. In the typical setting, $v_y = 4$ mm/s and $h_z = 4$ mm. The beam size is 2×2 mm, and the divergence of the beam is about 15". The aperture of the focal plane detector of the PC is a 12 mmΦ (7.4′) circle. Roughly 3% of the reflected photons fall outside this 7.4′ diameter circle, irrespective of the energy (see the later section about the image quality calibration), a factor which is not corrected in the tables and figures presented in this section.

3.1 *Optical Axis Distribution*

First, we determined the optical axis of the SXTs for the x-ray calibration with Ti-K 4.5 keV. We measured the EA for all the quadrants at off-axis angles of θ_y, $\theta_z = -4'$, 0, $+4'$ from the approximate optical axis of the whole telescope with optical parallel beams. The peaks fitted with the three-point data of θ_y and θ_z directions are defined as the optical axis on the respective coordinate axis. Figure 3 shows the results for the quadrant axis and the whole-telescope axis. The distribution of the measured optical axes among the quadrants is ∼30″ wide. The distribution in the SXT-S is narrower than that in the SXT-I.

3.2 *On-Axis Effective Area*

We measured the EA of the quadrants of the SXT-I and SXT-S at the whole-telescope axis (on-axis) with seven energies (Al-K 1.5 keV, Ti-K 4.5 keV, Cu-Kα 8.0 keV, Pt-Lα 9.4 keV, Pt-Lβ 11.1 keV, Pt-Lγ 12.9 keV, and Mo-K 17.5 keV). Figure 4 and Table 3 summarize the results. For comparison, those of the Suzaku XRT-I are also included. The characteristics of the EA are found to vary significantly from quadrant to

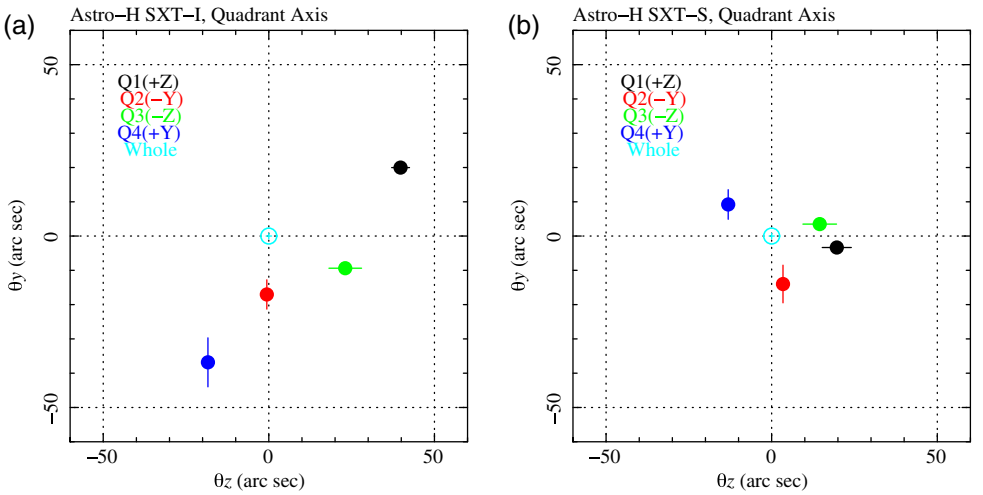

Fig. 3 Distribution of the optical axes among the quadrants in the (a) Astro-H SXT-I and (b) Astro-H SXT-S, measured at 4.5 keV. The origin of the coordinate axes is the whole-telescope axis. Short and long error bars correspond to the directions of the steeper and flatter angular responses, respectively.

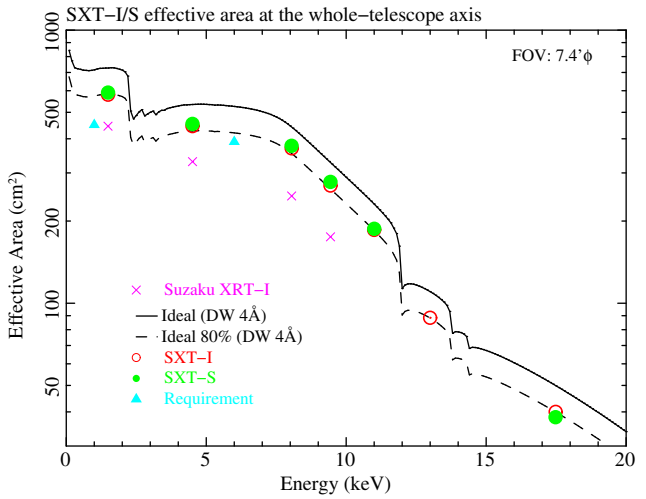

Fig. 4 EA per telescope of the Astro-H SXT-I and SXT-S at the whole-telescope axis. The system requirement of the SXT and the average value of Suzaku XRT-Is are also plotted. The solid and dashed curves show the ideal EA and the 80% of that calculated from the design parameters, respectively.

quadrant. For example, Q4(+Y) of SXT-I and Q3($-Z$) for SXT-S have a relatively low EA, irrespective of x-ray energies.

We find that the EA is ∼80% of the ideal value irrespective of the energy (Fig. 4). The ideal value is calculated with the design parameters and the reflectivity with the roughness of 4 Å. We adopted the Debye–Waller model for the reflectivity calculation and coded the formula by the Debye–Waller. During the calculation, we refer to the optical constant of the HENKE table. The total EA of the SXT-S is slightly larger than that of the SXT-I by ∼2%. The loss of ∼20% is not due to the test configuration on ground but due to deficiency of the telescope modeling. Misaki et al.[20] discussed the cause of the deficiency for the ASTRO-E XRTs. The cause of the loss will be in part due to the nonperfect shape of each reflector in which some fraction of the reflected x-rays with a large angle due to the figure error hits the back of the inner reflector. The similar loss is also occurred with nonperfect positioning of the reflector. The loss of ∼20% in the SXT EA can be qualitatively explained with a similar cause with the ASTRO-E XRTs.

Compared with the XRT-Is of Suzaku, the EA of the SXTs is larger by factors of ∼1.3 and ∼1.5 at 1.5 and 8.0 keV, respectively. This improvement is mainly due to the scale up of the diameter from 40 to 45 cm and of the focal length from 4.75 to 5.6 m.

Considering the EA of a telescope, the distribution of the quadrant axes is important. We measured the EA at each quadrant axis at 4.5 keV and show the results in Table 4. The sum of the EA of the quadrant is almost the same as the EA of the full telescope. This result implies that the optical axes of the four quadrants in SXT-I and SXT-S are well co-aligned.

3.3 *Off-Axis Effective Area (SXT-I)*

The SXT-I is for the SXI detector, which has a large detector-limited FoV ($38' \times 38'$). We measured the angular response at wide off-axis angles. First, we measured the EA at off-axis angles from $-4'$ to $4'$, scanning the full-telescope, at 4.5 keV. The measurement points of two directions (θ_y and θ_z), where the telescope is accordingly tilted to incident x-rays, are shown in Fig. 5. The data are fitted with a Lorentzian function with a full-width at half-maximum (FWHM) of $15.8'$. The residual in the best-fit results is found to be a few percent irrespective of the tilted direction.

Next, we measured the EA at wide off-axis angles up to $32'$, scanning the quadrant Q1(+Z) at the multiple energies (1.5, 4.5, 8.0, 9.4, 11.1, 12.9, and 17.5 keV). Figure 6 shows the result. The data are found to be well fitted with the model of a Lorentzian function but not with a Gaussian model. The residual to the best-fit model is typically 5% at smaller off-axis angles and energies, whereas it increases toward larger off-axis angles or larger energies [Fig. 6(c)]. The SXT FoV is $15.7'$ in FWHM at 1.5 keV, decreasing with higher x-ray energies, and is $6.2'$ at 17.5 keV. The vignetting width in full width at 90% maximum of the EA is within $5.2'$ and $2.1'$ at 1.5 and 17.5 keV, respectively. Although the vignetting measurement was made only for one quadrant and one direction, the vignetting of the whole telescope must be in the similar shape because the tilt directions are

Table 3 EA of all the quadrants measured at whole-telescope axis in unit of cm^2.

Quadrant (config)	1.5 keV	4.5 keV	8.0 keV	9.4 keV	11.1 keV	12.9 keV	17.5 keV
SXT-I Q1 (+Z)	147.7 ± 0.5	113.1 ± 0.5	92.0 ± 0.3	67.6 ± 0.3	46.2 ± 0.2	22.7 ± 0.2	10.8 ± 0.1
SXT-I Q2 (−Y)	146.8 ± 0.5	112.0 ± 0.5	94.0 ± 0.3	68.8 ± 0.3	47.8 ± 0.2	22.9 ± 0.2	10.1 ± 0.1
SXT-I Q3 (−Z)	150.3 ± 0.5	112.2 ± 0.5	94.9 ± 0.3	69.3 ± 0.3	48.1 ± 0.2	22.9 ± 0.2	10.2 ± 0.2
SXT-I Q4 (+Y)	140.6 ± 0.5	107.9 ± 0.4	88.3 ± 0.3	64.0 ± 0.2	43.5 ± 0.2	20.0 ± 0.2	8.9 ± 0.1
SXT-I total	580.4 ± 1.1	445.2 ± 0.9	369.1 ± 0.7	269.7 ± 0.5	185.5 ± 0.4	88.5 ± 0.5	40.0 ± 0.2
SXT-S Q1 (+Z)	149.4 ± 0.6	114.3 ± 0.5	95.4 ± 0.3	67.6 ± 0.3	46.0 ± 0.2	—	8.9 ± 0.1
SXT-S Q2 (−Y)	152.6 ± 0.5	116.6 ± 0.5	97.6 ± 0.3	71.3 ± 0.3	48.6 ± 0.2	—	10.6 ± 0.1
SXT-S Q3 (−Z)	142.1 ± 0.5	110.0 ± 0.5	89.1 ± 0.2	68.0 ± 0.3	44.2 ± 0.2	—	8.7 ± 0.1
SXT-S Q4 (+Y)	146.5 ± 0.5	112.7 ± 0.5	95.2 ± 0.3	71.2 ± 0.3	48.6 ± 0.2	—	10.1 ± 0.1
SXT-S total	590.6 ± 1.0	453.6 ± 1.0	377.2 ± 0.6	278.1 ± 0.5	187.5 ± 0.4	—	38.3 ± 0.2
SXT-S/I ratio	1.018 ± 0.002	1.019 ± 0.003	1.022 ± 0.002	1.031 ± 0.003	1.011 ± 0.003	—	0.955 ± 0.007
Suzaku XRT-I	~445	~330	~247	~175	—	—	—

Table 4 EA of the quadrants measured at each quadrant axis in unit of cm^2 at the energy of 4.5 keV. The rows of "ratio QT/full" list the ratio of the EA at each quadrant axis to that at full-telescope axis.

Quadrant (config)	Q1 (+Z)	Q2 (−Y)	Q3 (−Z)	Q4 (+Y)	Total
SXT-I	113.9 ± 0.4	111.3 ± 0.4	112.3 ± 0.4	108.1 ± 0.4	445.6 ± 0.8
Ratio QT/Full	1.006 ± 0.005	0.994 ± 0.005	1.001 ± 0.005	1.002 ± 0.005	1.001 ± 0.003
SXT-S	113.8 ± 0.5	116.2 ± 0.4	109.7 ± 0.5	113.4 ± 0.4	453.1 ± 0.9
Ratio QT/full	0.995 ± 0.005	0.997 ± 0.006	0.998 ± 0.006	1.006 ± 0.006	0.999 ± 0.003

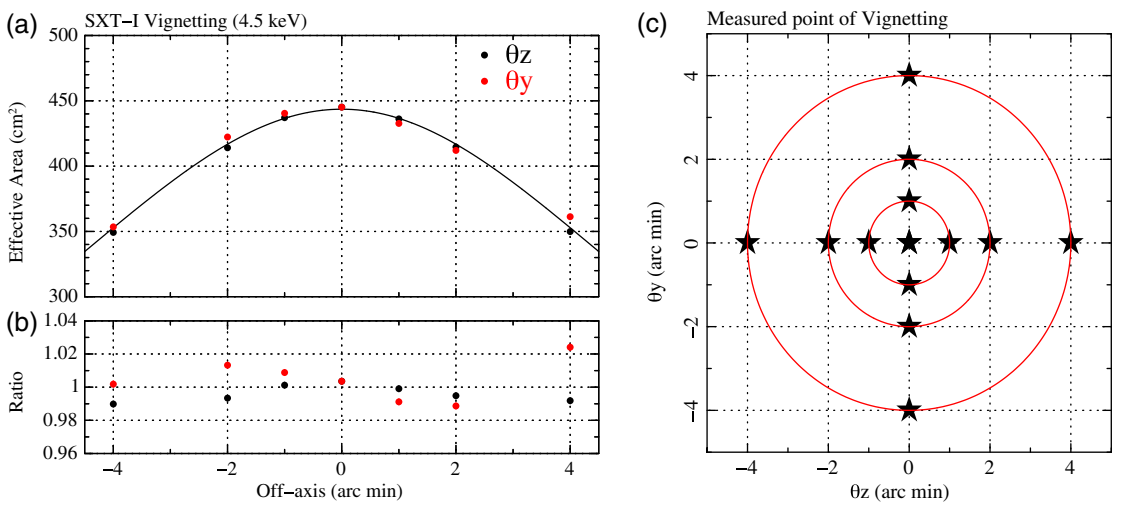

Fig. 5 (a) Total off-axis EA (vignetting function) of the four quadrants of the Astro-H SXT-I at 4.5 keV. (b) The ratio is the measured data to the best-fit model of a Lorentzian function with a width of 15.8′ (FWHM). (c) Measurement points are plotted for the two directions of tilt of the telescope to x-ray beam.

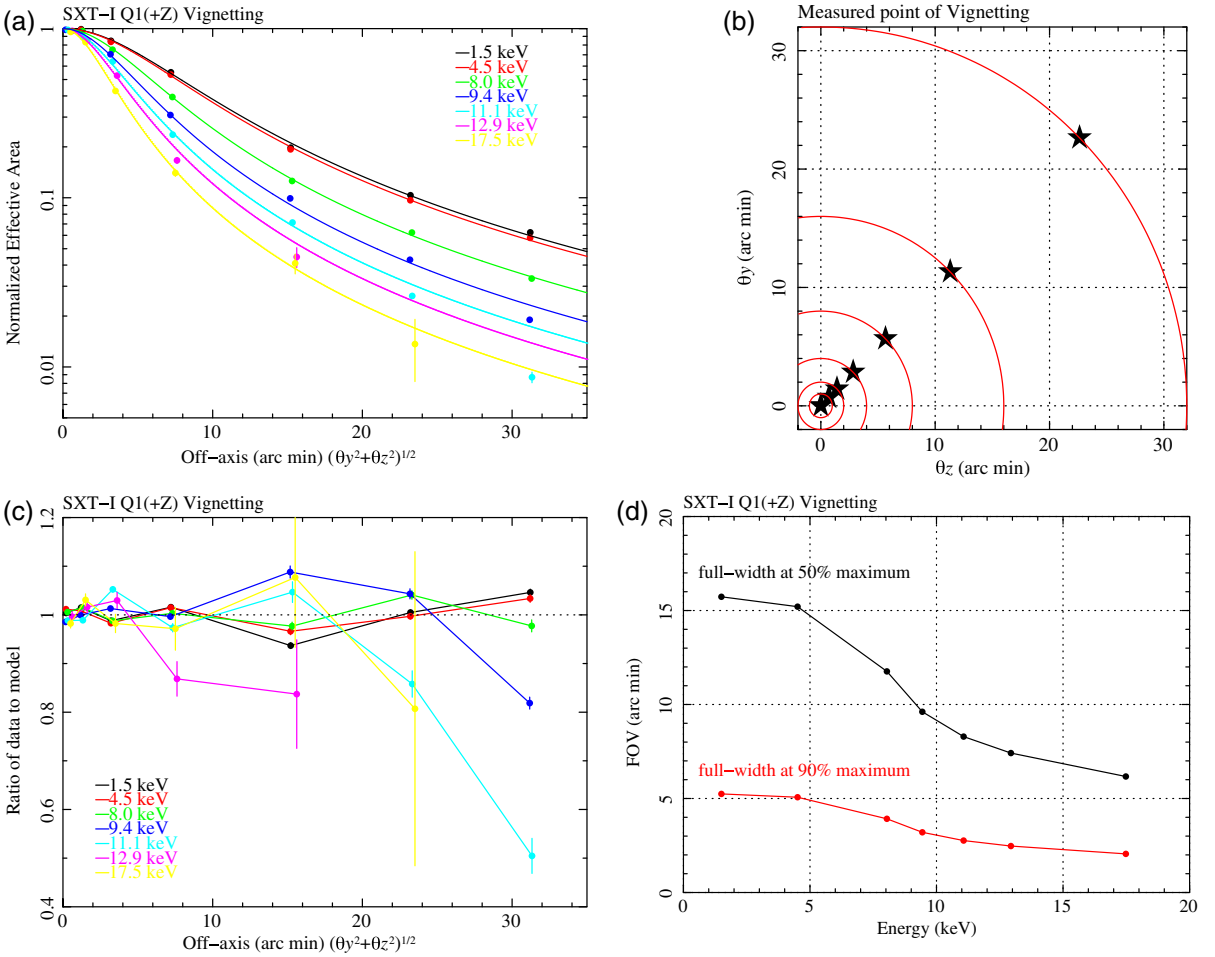

Fig. 6 (a) Off-axis EA (vignetting function) of the quadrant Q1$(+Z)$ of SXT-I at the multiple energies (1.5, 4.5, 8.0, 9.4, 11.1, 12.9, and 17.5 keV). The solid line is the best-fit model fitted by a Lorentzian function. The data are normalized with the peak value of the Lorentzian function. (b) The figure shows the measurement points. The direction is intermediate between steep and flat angular responses. (c) Ratio of the data to best-fit model. (d) Vignetting width in full-width at 50% maximum (or FWHM) and 90% maximum evaluated from the best-fit Lorentzian parameters.

intermediate between θ_y and θ_z, or between steeper and flatter angular responses.

3.4 *Off-Axis Effective Area (SXT-S)*

We measured angular responses at a small off-axis angle at various tilt directions for the SXT-S. It is because the focal-plane detector SXS is so small that the FoV of the SXS system is limited by the detector size. First, we measured the EA at off-axis angles from $-4'$ to $4'$, scanning the full-telescope, at 4.5 keV. Figure 7(a) shows the results for the two tilt directions (θ_y and θ_z). We then fitted the data with a Lorentzian model and found the best-fit Lorentzian width to be $16.0'$ in FWHM, which is the same value as that for the SXT-I (Fig. 5). The residual in fitting is $\sim$1%.

Next, we measured the EA at $1'$ off-axis angle for four tilting points at energy bands of 1.5, 4.5, 8.0, 9.4, and 11.1 keV [Fig. 7(b)]. The residual to the best-fit model is typically a few percent, with an increasing trend toward larger energies. Finally, we measured the EA at $1'$ and $2'$ off-axis angles for eight tilting points at 4.5 keV [Fig. 7(c)]. The residual is $\sim$1%. From these results, we conclude that the narrow vignetting in the SXS FoV has a small scattering of 1% to 2%, regardless of the tilt directions and x-ray energies.

4 Image Quality

In this section, we present the measured results of the imaging capability of the Astro-H SXT-I and SXT-S.

4.1 *On-Axis*

The detailed results are described in Refs. 21 and 22. To summarize, the obtained HPDs of the full-telescope in the 1.5 to 17.5 keV band are $1.25'$ to $1.47'$ and $1.19'$ to $1.35'$ for the SXT-I and SXT-S, respectively. The angular resolution is almost independent of the x-ray energy but is marginally worse at higher energies. The trend is especially notable for the Q3$(-Z)$ quadrant of the SXT-I. More detailed measurement has been carried out with the spot scan in order to examine this trend further, as reported in Refs. 21 and 22.

By contrast, the angular resolution of the XRT-Is of Suzaku was $1.7'$ to $1.9'$ (HPD). The significant improvement in the angular resolutions from Suzaku to Astro-H comes primarily from the improvement in precision in the shape of the reflecting

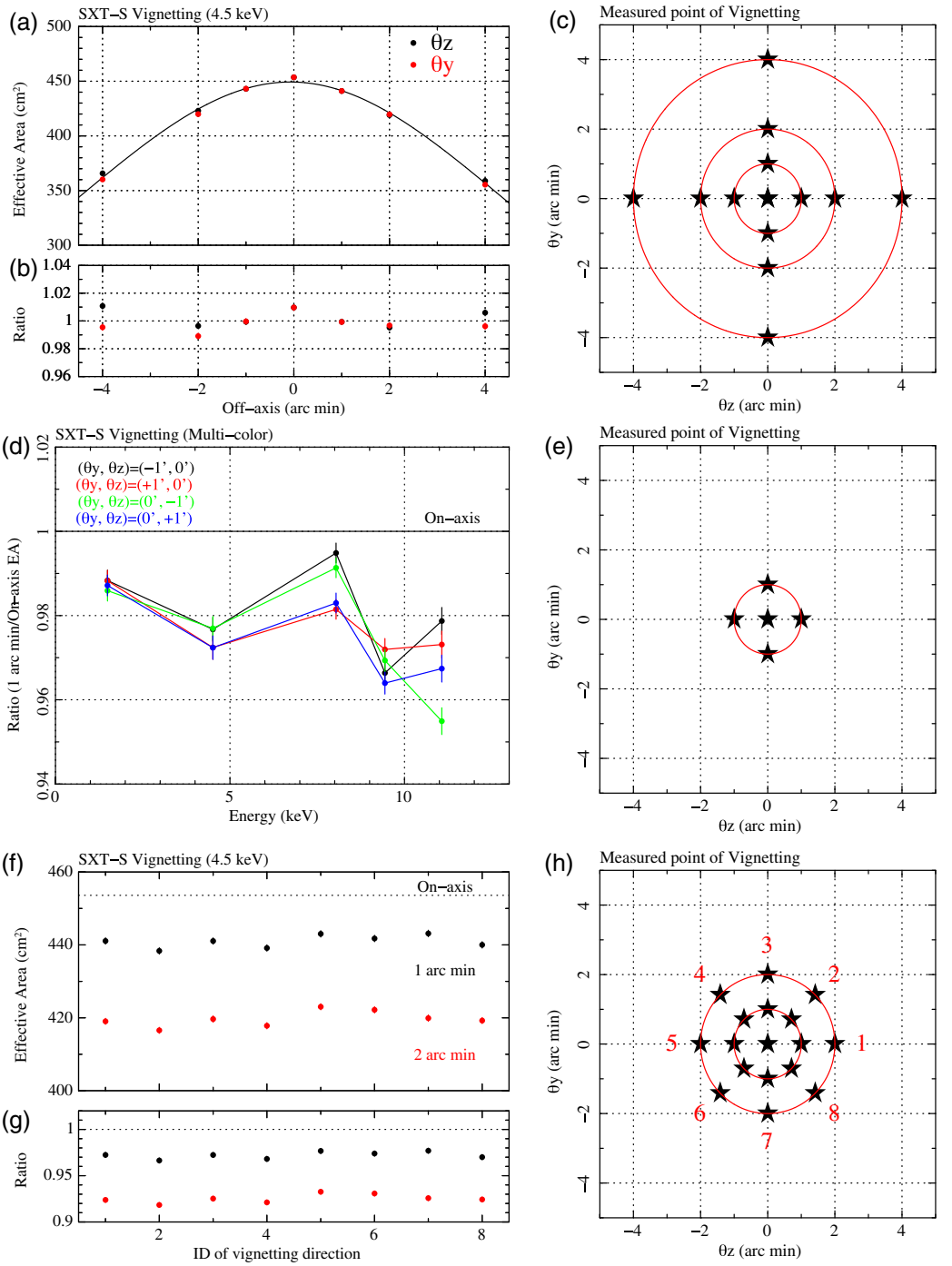

Fig. 7 (a) Off-axis EA of the SXT-S at 4.5 keV at −4′ to 4′ off-axis angles, tilting for two directions, at 4.5 keV. The ratio is the measured data to the best-fit Lorentzian model. (b) Off-axis EA at 1′ off-axis angle, tilting for four points, measured with multiple energies. The ratio is 1′ EA to that on the on-axis. (c) Off-axis EA at 1′ and 2′ off-axis angles, tilting for eight points, at 4.5 keV. The tilting directions are indicated with the ID numbers in the right panel.

surface and reflector positions.[5] The image quality with the Suzaku XRT-Is showed a large scatter from telescope to telescope due to a gravitation effect.[23] However, we find from the measurement of the rotation of the telescope of Q1$(-Z)$ that the gravitation effect causes no change in the optical axes or the image quality of the Astro-H SXTs. This improvement may be due to the fact that the reflectors are glued to the alignment bars in the Astro-H SXTs, whereas they were not in the Suzaku SXTs.

4.2 *X-Ray Scattering into the SXS FoV*

Because of the narrow detector-limited FoV of the SXS and the moderate angular resolution of the SXT-S, a significant fraction of the photons collected by the SXT-S does not fall onto the SXS even when the target source is located at the center of the SXS FoV. Figure 8 shows a SXT-S/SXS image of a point-like source located at the center of the FoV of the SXS. We estimated the EA for the SXS and its ratio to the EA with the circular FoV of a

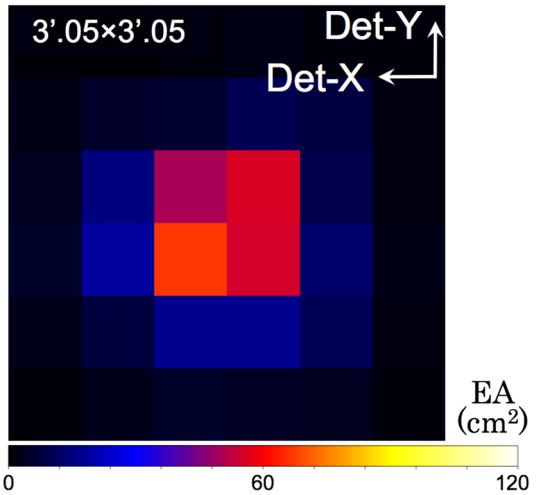

Fig. 8 Point-like source image of the SXT-S/SXS at 4.5 keV. The color level shows the EA per pixel in units of cm^2. DET-X and -Y in this figure denote the X and Y directions, respectively, in the detector coordinates of ASTRO-H.

diameter of 7.4′ (ISAS's PC 12 mmΦ), using the on-axis images of the SXT-S taken with the ISAS's CCD, and list them in Table 5 at six energy bands. We find the ratio to be ∼90% and to hardly depend on the energy (91% to 88% at 1.5 to 17.5 keV).

The fact that a significant fraction of the collected photons misses the SXS detector-limited FoV means that a significant amount of the flux from a source just outside the detector's FoV. We estimated the amount of the contamination, from sources at three off-axis angles of 3′, 4.5′, and 8.6′. For the 3′ off-axis image, the source is shifted from the on-axis in the perpendicular direction to the SXS, and for the 4.5′ and 8.6′, the sources are shifted in the diagonal direction, as demonstrated in Fig. 9. In the cases of 3′ and 4.5′ off-axis sources at 4.5 keV, we placed the off-axis source at four different positions, rotated for 90 deg, and measured the EA for each configuration. Table 6 shows the resultant EAs with the off-axis sources.

The 4.5-keV EA due to sources outside the detector FoV is 7.4 to 10.5 and 2.2 to 2.8 cm^2 at off-axis angles of 3′ and 4.5′, respectively, and hence to slightly depend on the off-axis angle. These EAs correspond to ∼2% and ∼0.6% of the on-axis EA, respectively. The ratio of the EA to that of on-axis sources does not depend on the energy with errors ∼0.5%. The EA for a highly off-axis source at an off-axis angle of 8.6′ is ∼0.1% of the on-axis EA.

4.3 *Large Off-Axis in the SXI FoV*

The SXI has a large detector-limited FoV of 38′ × 38′, and thus, the images at off-axis angles more than the half width of the SXI

Table 5 On-axis EA for the SXS and its ratio to the circular FoV of Φ7.4′ in diameter.

Energy (keV)	1.5	4.5	8.0	9.4	11.1	17.5
EA (cm^2)	535	412	340	251	169	34
Ratio (%)	91	91	90	90	90	88

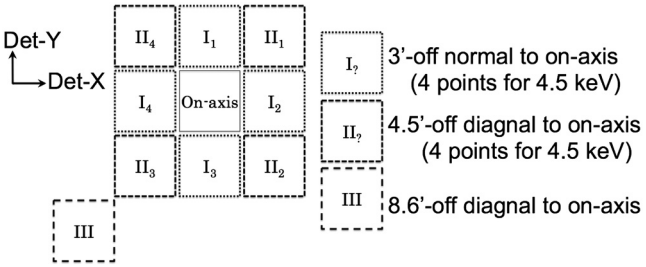

Fig. 9 Configuration of the source positions in the calibration work to estimate the EA of the off-axis sources for the SXS.

Table 6 EA of SXS for sources outside its FoV at 1.5/4.5/8.0 keV.

Off-axis (arc min) and position[a]	EA (cm^2)	Ratio (%)
3.0 (I-1)	9.2	2.2
3.0 (I-2)	7.4	1.8
3.0 (I-3)	6.6/7.4/5.7	1.2/1.8/1.7
3.0 (I-4)	10.5	2.6
4.5 (II-1)	2.2	0.5
4.5 (II-2)	2.8	0.7
4.5 (II-3)	2.2/2.4/2.0	0.4/0.6/0.6
4.5 (II-4)	2.2	0.5
8.0 (III)	0.4	0.1

[a]Position label defined in Fig. 9.

FoV should be investigated. Figure 10 shows images at off-axis angles between −4.5′ and 27′, where the positive is defined as in the direction of (DET-X, DET-Y) = $(+1/\sqrt{2}, +1/\sqrt{2})$. The EA and image quality (HPD) for the off-axis sources with the off-angles are tabulated in Table 7. We find that the image shrinks along the tilting direction and its opposite, the EA becomes smaller, and HPD becomes larger, as the off-axis angle increases, presumably because of the vignetting effect. Above 13.5′ of off-axis angle, a fan-shaped stray-light structure appears in the opposite side of the tilting direction to the image center. The surface brightness of the stray-light structure is $\sim 10^{-3}$ of that of image center. The details are described in the next section.

5 Stray Light

Although the FoV of the SXTs is ∼16′ in FWHM (Secs. 3.2 and 3.3), x-rays from outside of the FoV can reach the focal plane without experiencing the double reflection as they should be in the ideal Wolter-I type optics, because the thin-foil-nested mirrors used in the SXTs do not completely block the light paths of those kinds. The component makes a ghost image and is referred to as "stray light." In order to cut off the stray light as much as possible, a "precollimator" is installed on the top of each SXT.[8] The precollimator is composed of a thin and conical blade attached in front of the each primary reflector. The blade effectively blocks the light pass with an incident angle of about 30′ or larger on the plane (or radial) direction. The precollimator

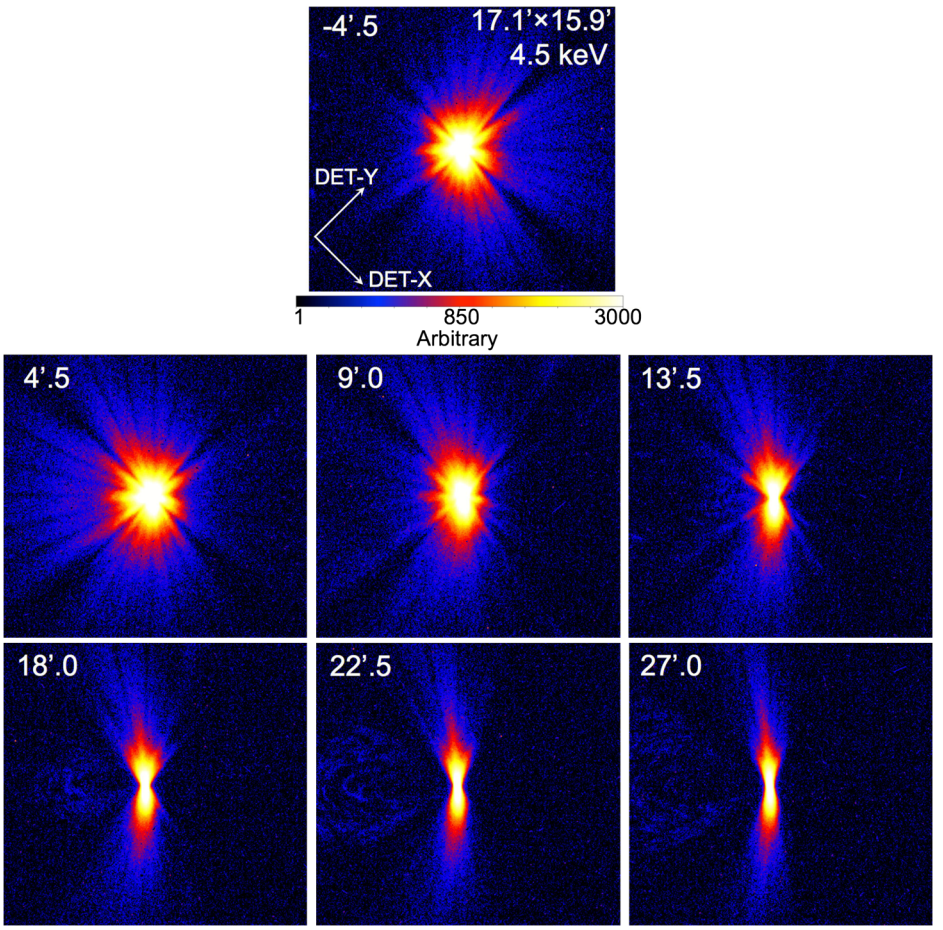

Fig. 10 SXT-I image of off-axis (−4.5′ to 27′) point-like sources with the FoV of 17.1 × 15.9 arc min^2.

Table 7 SXT-I EA (Φ7.4′) and image quality (HPD) for off-axis sources.

Off-axis (arc min)	−4.5	0	4.5	9.0	13.5	18.0	22.5	27.0
EA at 4.5 keV (cm^2)	328	445	343	213	134	99	77	64
Ratio (%)[a]	73.7	(100)	77.1	47.9	30.1	22	17	14
HPD (arc min)	1.18	1.26	1.24	1.29	1.43	1.58	1.72	1.87

[a]Ratio of the EA to the on-axis one with the same FoV.

significantly reduces the light pass of the nondouble reflection in the mirror modules.

In order to calibrate the stray lights, we, in advance, examined the light pass of the strays using the ray-tracing code. We then pick up three cases and made measurements as given as follows. The first and second is picked up for the SXT-I/SXI system while the third is for the SXT-S/SXS.

5.1 *On-Axis in the SXI FoV*

Figure 11 is an image of an on-axis point-like source with the FoV of 34′ × 34′. The image is a mosaic of four maps taken with the 17′ × 16′ CCD used in the ISAS beamline.

The image clearly shows a ring-like stray-light structure with the radius of 18′ around the image center. This stray is constructed by the photons reflected by only the innermost secondary reflectors and is identified as the unique stray pass at on-axis. Its surface brightness is very low and ∼10^{-5} of that of the image center.

5.2 *30′ Off-Axis in the SXI Detector-Limited FoV*

Due to the time limitation, we carried out the measurement at two representative off-axis angles of ±30′ only. The stray light at the other off-axis angles is then deduced via ray-tracing simulation, which is calibrated with the ±30′ off-axis angle data.

First, we took images, irradiating x-rays on only one quadrant at off-axis angles of ±30′ at 1.5 keV. In this measurement, the detector was placed at a distance of 3.733 m from the telescope (2/3 of the focal length) in order to reduce the number of

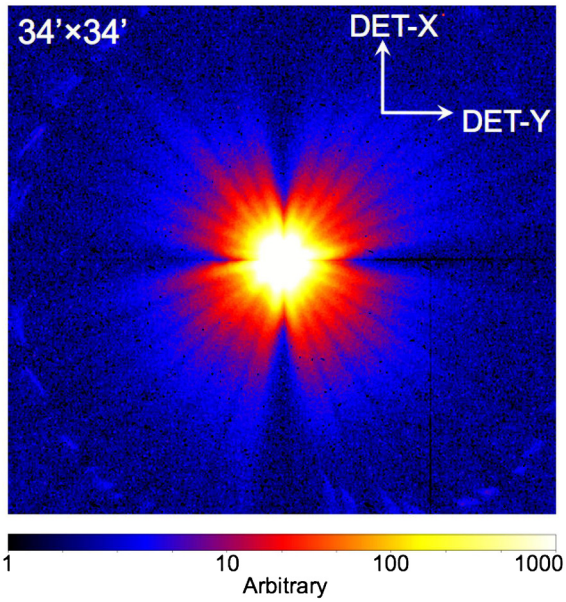

Fig. 11 SXT-I image of an on-axis point-like source with the FoV of 34×34 arc min^2. The ring-like structure with the radius of $18'$ around the image center is stray light (photons reflected only by the innermost secondary reflectors). Note that the color level in the image is saturated at around the center region.

mosaic mapping, and images were taken at three or four offset positions from the telescope's on-axis focus in order to cover the entire SXI FoV.

Figures 12(a) and 12(b) show the resultant images at the off-axis angles of $+30'$ and $-30'$, respectively. In the $+30'$ off-axis image, we identify some stray light components [e.g., the secondary-mirror single reflection, the direct component (no reflection), the backside-of-the-mirror reflection, and the precollimator reflection]. In the $+30'$ off-axis image, the backside-of-the-mirror reflection and precollimator reflection are marginally visible. We also estimate the EAs at the circular regions indicated in Fig. 12 (1S, 2S, 1B, and 2B), and list them in Table 8. Among them, the 2S region is found to be brightest with the EA of $\sim$0.59 cm^2, which is $\sim 10^{-3}$ of the on-axis EA of the full telescope. This region is dominated by the secondary-mirror single reflection component.

Next, we constructed an image, combining four images to cover the SXI FoV, each of which was illuminated for the entire telescope aperture at an off-axis angle of $30'$ [Fig. 12(c)]. The illuminating x-ray beam is tilted toward one of the boundaries of the quadrants. The detector was placed at the focal point (5.6 m from the telescope). We find in the resultant image only the direct component within the FoV. The other stray-light components are absent in the image, presumably because there are no reflectors or precollimators at the quadrant boundary.

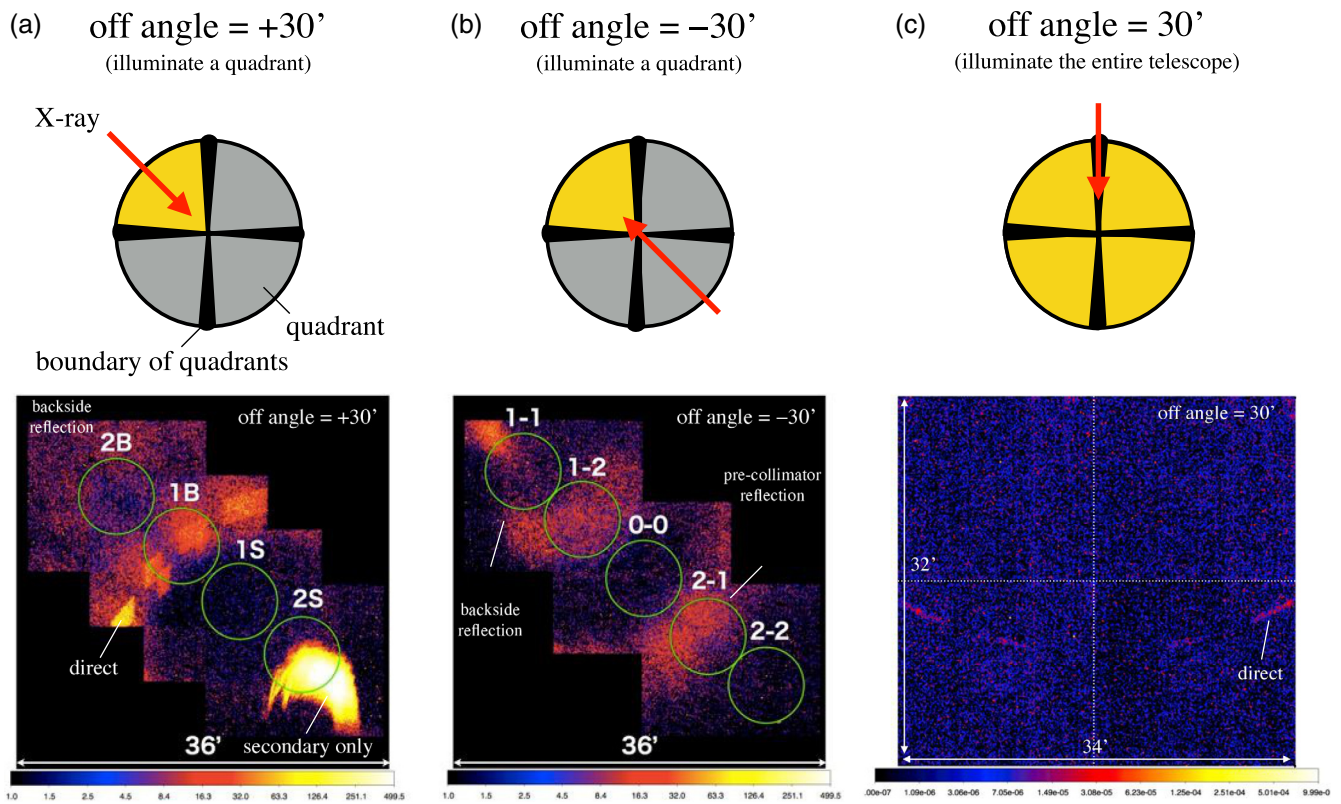

Fig. 12 (a) A quadrant SXI image at an off-axis angle of $30'$ at 1.5 keV. We took four offset images, shifting the CCD camera to cover the almost entire FoV of the SXI. The green circles (1S, 2S, 1B, and 2B) indicate the regions, for which we estimate the EAs (see Sec. 5.2 and Table 8). The texts indicate the primary origin of each stray feature. (b) Same as the left panel but at an off-axis angle of $-30'$, indicating five sets of circular regions (0-0, 1-1, 1-2, 2-1 and 2-2). (c) Image of the entire telescope at an off-axis angle of $30'$.

Table 8 EA of the SXT-I at an off-axis angle of ±30′ at 1.5 keV at several regions (see Fig. 12 for region IDs).

	Off-angle = +30′				Off-angle = −30′				
Region ID	1S	2S	1B	2B	0-0	1-1	1-2	2-1	2-2
EA (cm^2)	0.01	0.59	0.07	0.03	0.01	0.02	0.04	0.05	0.00

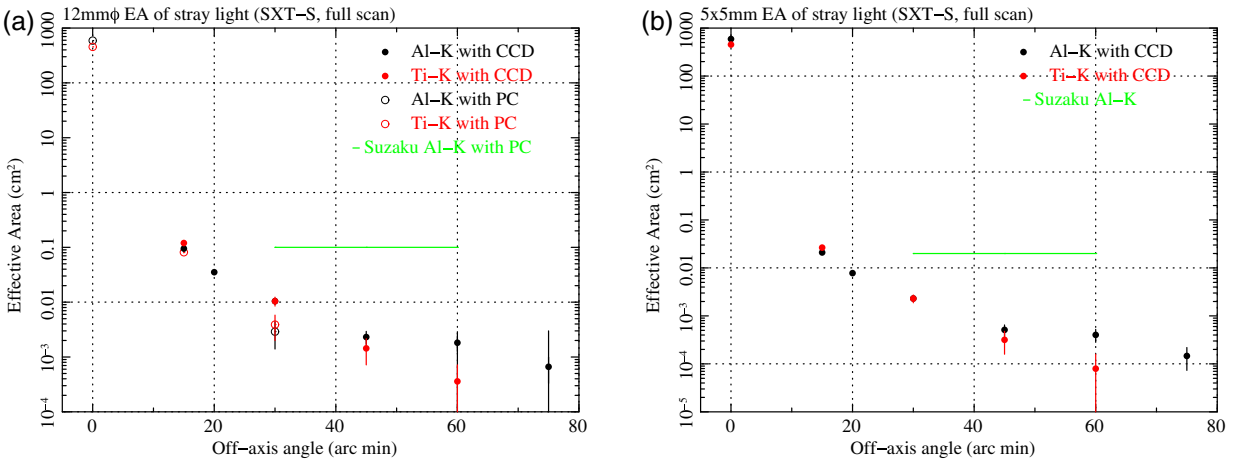

Fig. 13 (a) EAs at off-axis angles $\theta = 15'$, $20'$, $30'$, $45'$, $60'$, and $75'$ within the ISAS PC's FoV (12 mmΦ) with the PC (in open circles) and CCD (filled circles) at Al-K (1.5 keV, black) and Ti-K (4.5 keV, red). The green line shows the stray-light level of the Suzaku XRT-Is measured with the same PC at 1.5 keV. (b) Same as panel (a), but for the EA integrated over the SXS's FoV (5 × 5 mm). The green line shows the Suzaku level scaled from the results within 12 mmΦ.

5.3 *Strays in the SXS Detector-Limited FoV*

We studied the stray-light structures, illuminating the entire aperture of the SXT-S. We used both the CCD and the PC of the beamline, placing them at the on-axis focus, and used Al-K (1.5 keV) and Ti-K (4.5 keV). Figure 13 summarizes the EAs at off-axis angles of $\theta = 15'$, $20'$, $30'$, $45'$, $60'$, and $75'$, where, for the CCD results, we limited the photon integration region of the CCD to the same as the FoV of the PC. The results with the two kinds of detectors are found to be generally in good agreement. The EA of the SXS FoV at the off-axis angle of $30'$ is $(2.1 \pm 0.2) \times 10^{-3}$ cm^2 at 1.5 keV. The EA of the stray light at large off-axis angles ($>15'$) is $\sim 10^{-4}$ times smaller than the on-axis one ($\sim$590 cm^2). This implies that we can observe targets almost stray-light free; the contribution of stray lights is smaller than $\sim$1% with the SXS even if there is a contamination source that is 10 times brighter than the target at $15'$ off-axis.

For comparison, the EAs of stray lights for Suzaku are $\sim$0.1 and 0.02 cm^2 within the PC and SXS FoVs, respectively, at any of the off-axis angles $\theta = 30'$, $45'$, $60'$. at 1.5 keV. The stray-light level of the ASTRO-H SXTs from $30'$ to $60'$ is smaller than that of Suzaku XRT-Is by a factor of more than 10.

The reason of the reduction of stray lights from Suzaku to ASTRO-H is due to the small improvement in the aluminum substrate of the reflectors. We understand that the residual component of stray light with Suzaku XRT-Is is mostly the backside-of-the-mirror reflection after the precollimator has been introduced. To reduce the backside-of-the-mirror reflection, the scratch direction of the reflector substrate to the x-ray incident has been changed from parallel (Suzaku) to perpendicular (ASTRO-H). The surface with perpendicular scratches makes the reflectivity decrease by several orders of magnitude from that with parallel scratches. This method was adopted in the precollimator substrate of Suzaku.[24]

Note that we changed the height of the precollimator from Suzaku to ASTRO-H. It is to adjust the difference of the detector-limited FoV. The detector-limited FoV is $18'$ and $38'$ square for the Suzaku XRT-Is and the ASTRO-H SXT-I. To obstruct the stray light pass to the far edge of the SXI detector, we need to increase the height of the SXT-I precollimator.

6 Summary

We have presented our results of the ground calibration of the Astro-H SXTs at the ISAS/JAXA 30 m x-ray beam facility. The measurements were carried out by means of the raster scan method with a narrow x-ray pencil beam with a divergence of $15''$. We find that the EA, image quality, and stray-light contamination for both on-axis and off-axis sources meet requirements for both the SXT-I and the SXT-S. All the parameters with the SXT-S are slightly better than those with the SXT-I.

We also have compared the performance of the SXTs with that of the Suzaku XRTs. The angular resolution of the SXTs ($1.2'$ to $1.3'$ in HPD) was confirmed as significantly improved from the Suzaku XRTs ($\sim 2'$). The SXT-S stray lights in the SXS FoV are reduced by an order or more than the Suzaku XRT-S'.

Acknowledgments

This work was supported by JSPS KAKENHI under Grant Nos. 25870744, 25105516, 23540280, 26800113, 15J10520, and 17K05403.

References

1. T. Takahashi et al., "The ASTRO-H mission," *Proc. SPIE* **7732**, 77320Z (2010).
2. T. Takahashi et al., "The ASTRO-H x-ray observatory," *Proc. SPIE* **8443**, 84431Z (2012).
3. T. Takahashi et al., "The ASTRO-H x-ray astronomy satellite," *Proc. SPIE* **9144**, 914425 (2014).
4. T. Takahashi et al., "The ASTRO-H (Hitomi) x-ray astronomy satellite," *Proc. SPIE* **9905**, 99050U (2016).
5. Y. Soong et al., "ASTRO-H soft x-ray telescope (SXT)," *Proc. SPIE* **9144**, 914428 (2014).
6. T. Okajima et al., "First peek of ASTRO-H soft x-ray telescope (SXT) in-orbit performance," *Proc. SPIE* **9905**, 99050Z (2016).
7. P. J. Serlemitsos et al., "The x-ray telescope onboard Suzaku," *Publ. Astron. Soc. Jpn.* **59**, S9–S21 (2007).
8. H. Mori et al., "The pre-collimator for the ASTRO-H x-ray telescopes: shielding from stray lights," *Proc. SPIE* **8443**, 84435B (2012).
9. Y. Tawara et al., "Development of ultra-thin thermal shield for ASTRO-H x-ray telescopes," *Proc. SPIE* **8147**, 814704 (2011).
10. Y. Soong et al., "ASTRO-H soft x-ray telescope (SXT)," *Proc. SPIE* **8147**, 814702 (2011).
11. P. Gondoin et al., "Calibration of the first XXM flight mirror module: II. Effective area," *Proc. SPIE* **3444**, 290–301 (1998).
12. H. Kunieda et al., "Thirty-meter x-ray pencil beam line at the institute of space and astronautical science," *Jpn. J. Appl. Phys.* **32**, 4805–4813 (1993).
13. D. E. Zissa, "AXAF-1 high-resolution mirror assembly image model and comparison with x-ray ground-test image," *Proc. SPIE* **3766**, 36–50 (1999).
14. Y. Tsusaka et al., "Characterization of the advanced satellite for cosmology and astrophysics x-ray telescope: preflight calibration and ray tracing," *Appl. Opt.* **34**, 4848–4856 (1995).
15. Y. Maeda et al., "Soft x-ray calibration for the NeXT x-ray telescope," *Proc. SPIE* **7011**, 70112O (2008).
16. T. Okajima et al., "First measurement of the ASTRO-H soft x-ray telescope performance," *Proc. SPIE* **8443**, 844320 (2012).
17. T. Hayashi et al., "Upgrade of the 30-m x-ray pencil beam line at the Institute of Space and Astronautical Science," *J. Astron. Telesc. Instrum. Syst.* **1**, 044004 (2015).
18. K. Ichihara et al., "A ground calibration of the engineering model of the SXT onboard ASTRO-H using the ISAS 30m pencil beam facility," *Proc. SPIE* **8443**, 844357 (2012).
19. T. Hayashi et al., "Upgrade of the thirty-meter x-ray pencil beam line at the Institute of Space and Astronautical Science," *Proc. SPIE* **9144**, 91444A (2014).
20. K. Misaki et al., "x-ray telescope onboard Astro-E. III. Guidelines to performance improvements and optimization of the ray-tracing simulator," *Appl. Opt.* **44**, 916–940 (2005).
21. T. Sato et al., "Revealing a detailed performance of the soft x-ray telescopes of the ASTRO-H mission," *Proc. SPIE* **9144**, 914459 (2014).
22. T. Sato et al., "Examining the angular resolution of the ASTRO-H's soft x-ray telescopes," *J. Astron. Telesc. Instrum. Syst.* **2**(4), 044001 (2016).
23. A. Itoh et al., "Ground-based x-ray calibration of the Astro-E2 x-ray telescope: I. With pencil beam," *Proc. SPIE* **5488**, 93–102 (2004).
24. H. Mori et al., "Pre-collimator of the Astro-E2 x-ray telescopes for stray-light reduction," *Publ. Astron. Soc. Jpn.* **57**, 245–257 (2005).

Ryo Iizuka is a researcher of the Astro-H project team at the Institute of Space and Astronautical Science (ISAS) of Japan Aerospace Exploration Agency (JAXA). He received his MS and PhD degrees in astronomy from the University of Tokyo, Japan, in 2003 and 2006, respectively. His current main research interests are x-ray telescopes and x-ray polarimeters. He is not a member of SPIE.

Biographies for the other authors are not available.